PHYSICAL REVIEW B **68**, 235110 (2003)

Coupling between a point-defect cavity and a line-defect waveguide in three-dimensional photonic crystal

Makoto Okano,* Shinichi Kako, and Susumu Noda†
Department of Electronic Science and Engineering, Kyoto University, Kyoto 615-8510, Japan

(Received 4 June 2003; revised manuscript received 30 September 2003; published 18 December 2003)

The properties of the coupling between a point-defect cavity and a line-defect waveguide in three-dimensional (3D) photonic crystal are investigated theoretically using plane-wave expansion and 3D finite-difference time-domain methods. It is shown that for the symmetric structure where the point and line defects are on the same rod within the photonic crystal, a state is created in which the point- and line-defect modes are completely decoupled due to the mismatch in modal symmetry, while coupled states can be formed by introducing asymmetry. In these asymmetric structures, the strength of coupling between point- and line-defect modes is estimated as a function of the position of the end of the line-defect waveguide by estimating the quality factor of the point-defect cavity. The quality factor is found to oscillate with small changes in the position of the waveguide. For instance, the quality factor changes by a factor of up to $\sim 1.1\times 10^4$ with small positional change. In addition, the quality factor and light extraction efficiency are estimated when the size of the photonic crystal is finite, as in experimental circumstances. These findings provide very useful design rules for controlling the transfer of light from the point-defect cavity to the line-defect waveguide. These coupling structures are thought to be an important component in 3D photonic crystal optical circuits.

DOI: 10.1103/PhysRevB.68.235110 PACS number(s): 42.70.Qs, 42.60.Da, 42.82.Et, 42.55.Sa

I. INTRODUCTION

Over the last 15 years, there has been growing interest in the research of photonic crystal.[1–4] Photonic crystal is an artificial optical material with periodically varying refractive index and an energy range, called the photonic band gap (PBG), in which propagation of electromagnetic waves is disallowed in all directions. By introducing various defects into the photonic crystal, a variety of localized modes, such as resonant and waveguide modes,[3–6] are formed and various scientific and engineering applications, such as control of spontaneous emission,[7,8] zero-threshold lasing, and ultrasmall optical circuits,[9] will be possible.

Recently, remarkable results about three-dimensional (3D) photonic crystal which is referred to as layer-by-layer,[10,11] woodpile,[12] or stack-of-logs[3,13] structure have been reported. A photonic crystal consisting of III-V semiconductors such as GaAs and InP has been successfully fabricated and exhibited a complete photonic band gap at near-infrared wavelengths (1–2 μm).[3,14] A set of useful design rules for the construction of a single-mode high-Q optical cavity has been theoretically developed.[15] This photonic crystal has considerable potential for the creation of efficient light-emitting devices based on point-defect cavities. The next focus in the theoretical approach is on transfer of light from point defects. We especially focus on the light extraction by utilizing the line-defect waveguide. This design is considered as a very important component in 3D photonic crystal optical circuits. Line-defect waveguides themselves have already been investigated theoretically[16–18] and demonstrated experimentally at microwave wavelengths (around 25 mm).[19,20]

In this paper, we present a method of coupling a point-defect cavity to a line-defect waveguide to extract light from the cavity. Computational analysis of the coupling between the cavity and waveguide is performed using the plane-wave expansion method,[21,22] which is easily able to identify point- and line-defect modes, and the 3D finite-difference time-domain (FDTD) method,[23] which is able to simulate time responses of various structures. The properties of a variety of coupling structures are investigated and very useful guidelines for controlling the transfer of light from the point-defect cavity to the line-defect waveguide are presented.

II. METHODS OF COMPUTATIONAL ANALYSIS

Two numerical methods are used. The plane-wave expansion method, which involves solving Maxwell's equations in the frequency domain, is used to find the existence of point- and line-defect modes, and compute the frequency and field distribution of them. The supercell method and dense matrix techniques with the dielectric function computed via the inverse matrix method[24] are also used in calculations. The 3D FDTD method is then used to directly solve Maxwell's equations in the time domain and to calculate the frequency, field distribution, and time response of each defect and coupled mode. Line-defect modes are analyzed using the 3D FDTD method with periodic Bloch conditions at the lateral surfaces and Berenger's perfectly matched layer (PML) boundary conditions[25,26] applied to the top and bottom surfaces. To analyze point-defect modes and structures in which the point defect and the waveguide are coupled, the 3D FDTD method with Berenger's PML boundary condition applied to every surface is employed.

To reduce reflections from the end of the waveguide in coupled structures where electromagnetic waves propagate from the point defect to the waveguide, the waveguide is introduced into the PML medium, with electric conductivity modulated according to a relative dielectric constant $\varepsilon_r(\mathbf{r})$.

Note that in 2D FETD-BPM,[27] which is a unified time-domain beam propagation method based on the finite-element method, introduction of a 2D photonic crystal waveguide into PML media has been achieved with anisotropic PML boundary conditions.[28] PML media have electric and magnetic conductivities σ_x and σ_x^* in the *x* direction, σ_y and σ_y^* in the *y* direction, and σ_z and σ_z^* in the *z* direction, and matching conditions in air are expressed as

$$\frac{\sigma_i}{\varepsilon_0}=\frac{\sigma_i^*}{\mu_0} \quad (i=x,y,z). \tag{1}$$

The modulated electric conductivity then becomes

$$\sigma_j(\mathbf{r})=\varepsilon_{\mathrm{r}}(\mathbf{r})\sigma_{0j}(j)=\varepsilon_{\mathrm{r}}(\mathbf{r})\sigma_{j,\max}(j/d_j)^{n_j}, \tag{2}$$

where j corresponds to the direction of the waveguide, $\sigma_{0j}(j)$ corresponds to normal electric conductivity, $\sigma_{j,\max}$ is the normal electric conductivity at the perfect electric conductor (PEC) outer boundary $[\sigma_{0j}(d_j)]$, d_j indicates the thickness of the PML medium, and n_j is the polynomial grading order. Equation (2) can also be expressed as

$$\frac{\sigma_j(\mathbf{r})}{\varepsilon_0\varepsilon_{\mathrm{r}}(\mathbf{r})}=\frac{\sigma_{0j}(j)}{\varepsilon_0}=\frac{\sigma_j^*(j)}{\mu_0}. \tag{3}$$

Ostensibly, this is equivalent to the equation for multilayer planer structures.[29] In the case of 3D photonic crystal, however, $\varepsilon_{\mathrm{r}}(\mathbf{r})$ changes dynamically in all directions. A PML thickness as large as $9a$ (144 cells) is then used to negate reflection effects from the waveguide end, where *a* is the center-to-center distance of the rods (16 cells per *a*). Generally, in free space, PML media of 8–16 cells in thickness are used. The order n_j and $\sigma_{j,\max}$ are set 3 and $-\sqrt{\varepsilon_0}(n_j+1)\ln(10^{-6})/2d_j$, respectively. Moreover, a uniform dielectric material of thickness $2a$ is placed alongside the PEC wall to avoid divergence problems that sometimes occur due to coupling of photonic crystal with the PEC wall. Detailed results of the "photonic-crystal-buried Berenger's PML boundary condition" will be reported elsewhere.[30] Note that it has been confirmed that this can be applied similarly to a waveguide in 2D photonic crystal slab.

The plane-wave expansion method is good at revealing the presence of eigenmodes and easily yields the field patterns of all eigenmodes. However, the plane-wave expansion method which uses the supercell approach has some convergence problems that are attributable to an insufficient number of plane waves and the size of the supercell. Results obtained by the plane-wave expansion method are thus utilized to determine the light source and verify results of the FDTD analysis, while the FDTD method is the main theory used in calculations. In addition, the pair of band edge frequencies is calculated using the FDTD method with periodic Bloch conditions imposed at boundaries of the unit cell, and the plane-wave expansion method is used for light source identification and verification.

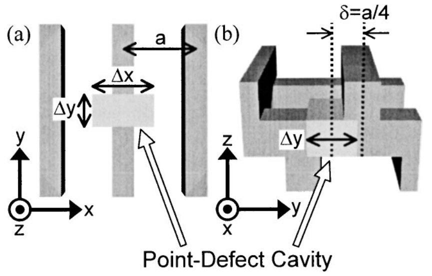

FIG. 1. Schematic of the point-defect optical cavity with $\Delta x=2\Delta y$ and shifted by $a/4$, formed by adding dielectric material to photonic crystal: (a) top view and (b) side view.

III. ANALYSIS OF ISOLATED POINT-DEFECT CAVITIES AND LINE-DEFECT WAVEGUIDES

In this paper, the parameters of the photonic crystal are chosen to be different from that in Refs. 15 and 16. In consideration of the fabricating method with the wafer-fusion technique[13] and the current injection, the width of the rod is widened, and the thickness of the rod is adjusted to maximize the PBG. The width and thickness of the rod are consequently equal to $0.3a$ and $0.3125a$, where a is the center-to-center spacing of the rods. The refractive index of the dielectric rod is assumed to be 3.375, corresponding to semiconductor materials such as GaAs. In this section we examine properties of an isolated point-defect cavity and line-defect waveguide in stack-of-logs structured 3D photonic crystal. Although the structure is different, the essence of these properties is already reported in Refs. 15 and 16. Therefore a small number of results, which are necessary to understand the properties of the coupling between a point-defect cavity and a line-defect waveguide, are shown in this paper.

A point-defect cavity, shown in Fig. 1, was examined. The defect is rectangular $(\Delta x=2\Delta y)$, is shifted $a/4$ from the position of the rod center in the adjacent layer, and has the same thickness as the rod within which it was embedded. Normalized frequencies of resonant modes in the point defect are shown in Fig. 2 as a function of defect size. Vertical

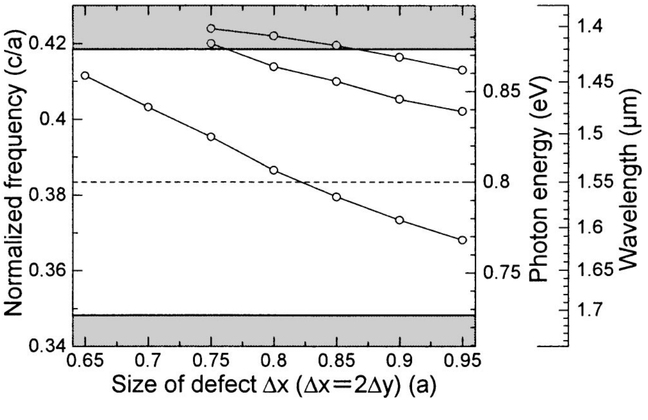

FIG. 2. Normalized frequency of the point-defect mode as a function of cavity size. Shaded areas indicate edges of the PBG. The dashed line indicates the middle frequency of the PBG. Frequency range of the PBG is $0.3483c/a$ to $0.4185c/a$.

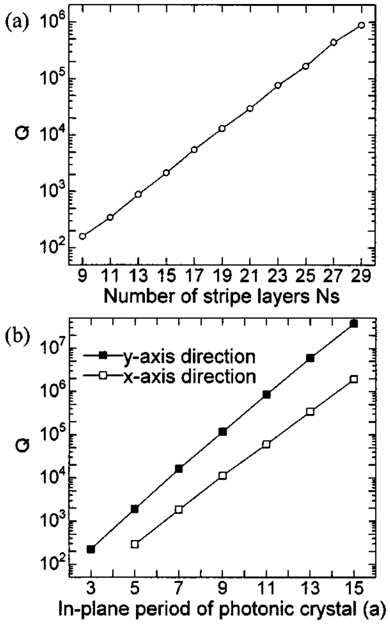

FIG. 3. Dependence of quality factor of the point-defect cavity ($\Delta x = 2\Delta y = 0.85a$) on (a) the number of stripe layers and (b) the in-plane size in the x-axis and y-axis directions.

axes on the right side of the graph indicate photon energy and wavelength, with photon energy (wavelength) in the middle of the PBG being 0.8 eV (1.55 μm). At this scale, a is approximately 0.6 μm. This shows that a wide defect-mode separation can be obtained (over 60 meV). We then investigate the quality factor Q of the point defect ($\Delta x = 2\Delta y = 0.85a$). Q is determined by measuring the decay constant of the electromagnetic field in the point defect.[31] The dependence of Q on the size of the photonic crystal is shown in Fig. 3, where the photonic crystal is surrounded by dielectric material with refractive index equal to that of the dielectric rod in the photonic crystal. In Fig. 3(a), the number of stripe layers, N_S, is changed, where one layer consists of one-dimensional stripe structure. The in-plane size is large enough, $19a \times 19a$ for $N_S \leqslant 19$ and $29a \times 29a$ for $N_S > 19$, to make the in-plane radiation losses negligible. On the other hand, in Fig. 3(b), one in-plane size is changed and the other size is fixed to $29a$. The vertical size is set enough large, $N_S = 81$ ($\sim 25a$). Q increases exponentially with the crystal size. These Q's are important to consider the radiation losses. This donor-defect cavity is suitable for the light-emitting devices, as this could be applied to the introduction of a light emitter into the dielectric material and single-mode operation is expected.

Next, a line-defect waveguide that is constructed by removing one rod from a photonic crystal[16] was investigated. Normalized frequencies of guided modes in the waveguide are shown in Fig. 4 as a function of wave vector, demonstrating that a single mode with a wide frequency range (85 meV) can be obtained. In addition, this kind of waveguide has high transmission efficiencies in a 90° bend and T-branch waveguides.[18,19] These properties are advantageous to ultrasmall optical circuits.

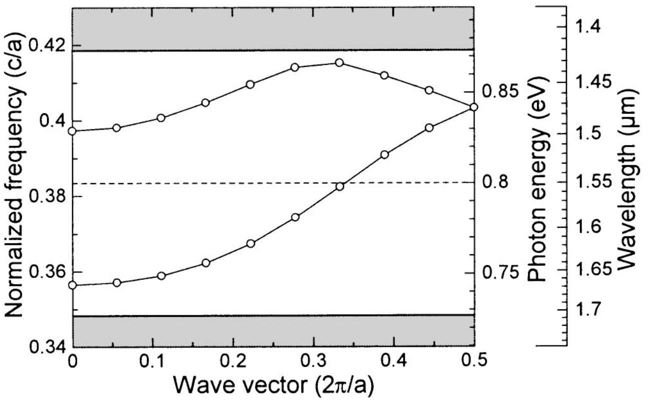

FIG. 4. Normalized frequency of the line-defect mode as a function of wave vector.

IV. ANALYSIS OF THE COUPLING BETWEEN POINT-DEFECT CAVITIES AND LINE-DEFECT WAVEGUIDES

We have investigated the coupling between the point-defect cavity and the line-defect waveguide described above. The point defect size is taken to be $\Delta x = 0.85a$ and $\Delta y = 0.425a$, giving a resonant frequency corresponding to the single-mode region of the line-defect waveguide. The point defect was excited by a pulse with a Gaussian time envelope and a time response of the electromagnetic field in the cavity was observed. Frequency was adjusted to couple only to the point-defect mode of interest. In this section, with the exception of Sec. IV E, the defect layer is sandwiched between a pair of 17-layer stacks, i.e., N_S is equal to 35. This is to reduce radiation losses in the vertical direction, so that losses from the point defect to the waveguide can be estimated.

A. Symmetric structure

First, the coupling structure shown in Fig. 5 was examined. The point defect and waveguide are placed on the same rod. Time response and field pattern at the middle of the defect layer were measured, and the field pattern is shown in Fig. 6. It is clear that light localized in the point defect does

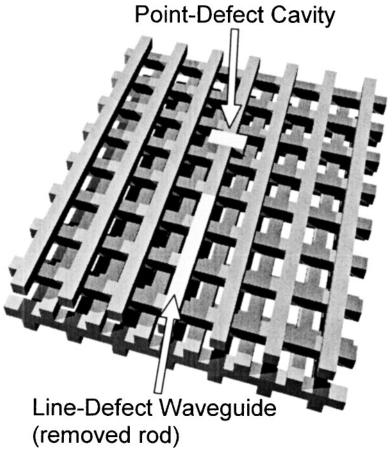

FIG. 5. Schematic of symmetric coupling structure with point and line defects located on the same rod.

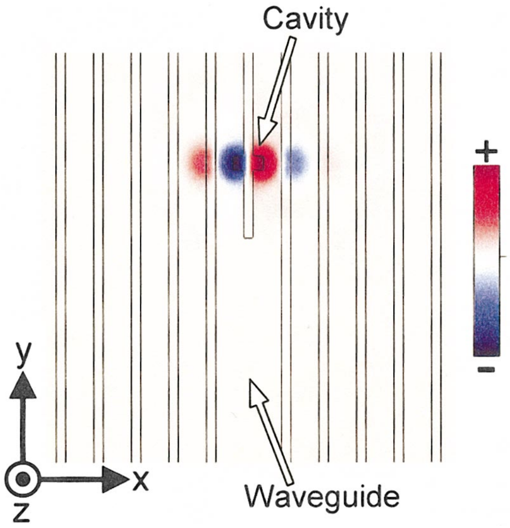

FIG. 6. (Color) Distribution of the electric field E_z across the middle of the defect layer in the structure shown in Fig. 5.

not propagate to the waveguide. Although separation between the center of the point defect and the end of the waveguide was varied from $1.5a$ to $3a$, the two modes were not found to couple. Field distributions of the point- and line-defect modes were then observed in an attempt to find the origins of the uncoupled state, as shown in Fig. 7. The coupling structure has a symmetry plane σ through the centers of the point defect and line defect. Mirror operator $\hat{\sigma}$ of electric field, which is a polar vector, can be expressed as

$$\hat{\sigma}\mathbf{E}(\mathbf{r},t)=R\mathbf{E}(R^{-1}\mathbf{r},t)$$
$$=(-E_x(-x,y,z,t),E_y(-x,y,z,t),E_z(-x,y,z,t)), \quad (4)$$

where R is the orthogonal matrix representation of the mirror operator $\hat{\sigma}$ and R^{-1} is the inverse matrix of R.[32] R is denoted by

$$R=\begin{pmatrix} -1 & 0 & 0 \\ 0 & 1 & 0 \\ 0 & 0 & 1 \end{pmatrix}. \quad (5)$$

It is clear that the field of the point defect is odd $[\mathbf{E}(\mathbf{r},t)=-\hat{\sigma}\mathbf{E}(\mathbf{r},t)]$, while that of the waveguide is even $[\mathbf{E}(\mathbf{r},t)=+\hat{\sigma}\mathbf{E}(\mathbf{r},t)]$. It is found out that the difference between the symmetries of the point- and line-defect modes makes it impossible for them to couple. Note that when the point- and line-defect modes have the same symmetry, the modes couple naturally.

B. Asymmetric structure

As has been demonstrated, an uncoupled state is formed due to the opposite parities of point- and line-defect modes about the symmetry plane. In an attempt to couple the two defect modes, asymmetry was introduced, as shown in Fig. 8, in which the waveguide is shifted a distance of $2a$ along the x axis to break symmetry. Asymmetry could also be formed by shifting the point defect, but this would lead to a reduction in the frequency separation of the point-defect modes. As importance is attached to properties of the point defect, the cavity structure is unchanged. The field pattern at the middle of the defect layer is shown in Fig. 9. This shows that the point-defect mode couples to the line-defect mode owing to the introduction of the asymmetry.

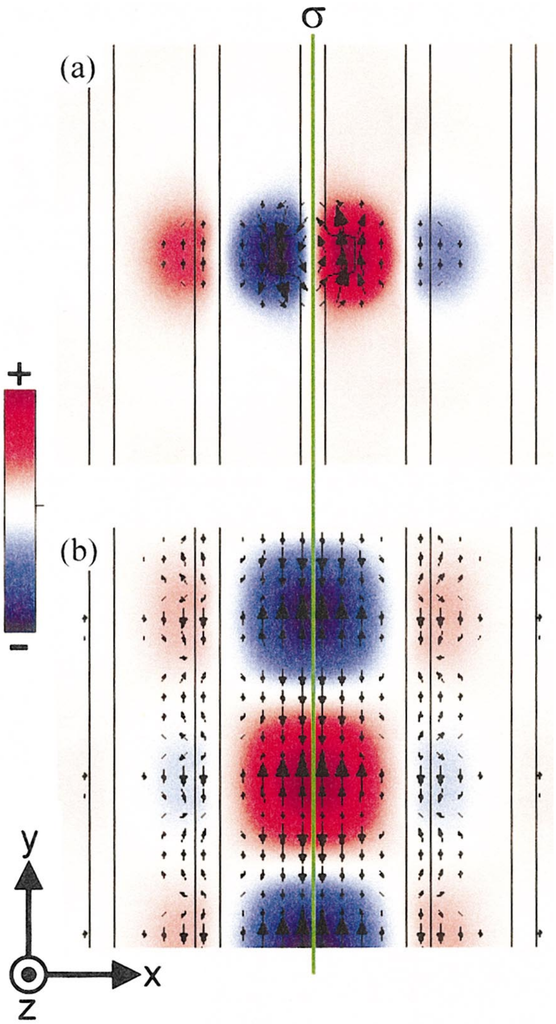

FIG. 7. (Color) Electric field distribution across the middle of the defect layer for (a) the point-defect mode and (b) the line-defect mode. The vector and color plots show E_{xy} and E_z, respectively. σ indicates the symmetry plane of each defect structure.

C. Coupled states in asymmetric structures

Coupling strength of point- and line-defect modes as a function of distance of the waveguide from the point defect was investigated. Coupling strength was estimated by measuring quality factor Q of the point defect. Q is defined as

$$Q=\omega_0\frac{\text{stored energy}}{\text{power loss}}, \quad (6)$$

where ω_0 is the resonant angular frequency.[32] Power loss from the point defect is assumed to be entirely due to energy

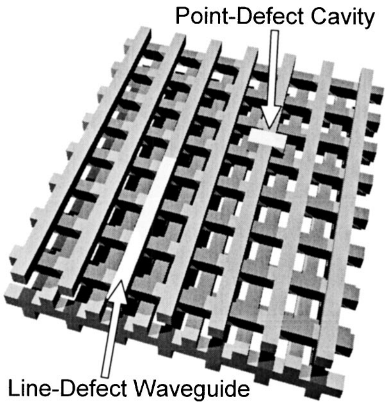

FIG. 8. Schematic of asymmetric structure where the point-defect cavity and the line-defect waveguide are separated by an intervening rod.

propagating into the waveguide because the point defect is surrounded by enough photonic crystal to prevent radiation losses. Therefore, coupling strength is inversely proportional to *Q*.

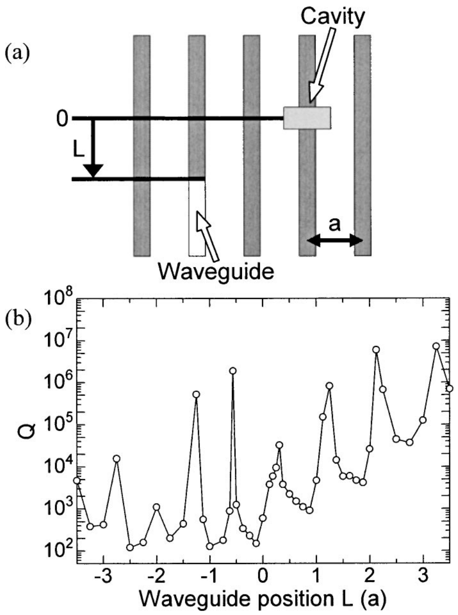

FIG. 10. (a) Schematic of the structure containing a point-defect cavity and a line-defect waveguide separated by an intervening rod. The definition of *L*, as the distance between the point defect and the waveguide is illustrated. (b) Quality factor as a function of *L* for the structure in (a).

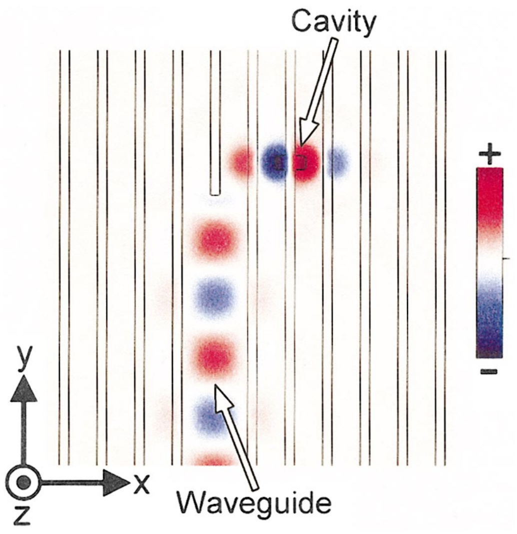

FIG. 9. (Color) Distribution of the electric field E_z across the middle of the defect layer for the structure shown in Fig. 8.

The position of the line-defect waveguide, *L*, is defined as shown in Fig. 10(a). Figure 10(b) shows *Q* as a function of *L* where *L* changes from $-3.5a$ to $3.5a$. The in-plane size of the photonic crystal is $23a\times 43a$, where the edge of the photonic crystal in the $-y$-axis direction is introduced into the PML medium as described in Sec. II. The center of the point defect is placed at $(12.5a,-12.5a)$, setting the origin of the coordinate axes the upper left corner of the photonic crystal. The in-plane size is large enough to diminish radiation losses in the in-plane direction, and the length in *y* direction is long enough for the line-defect mode to become the stable state before propagating into the PML medium. It can be seen that *Q* is oscillatory, with small changes in *L* leading to large changes in *Q*. For example, a $\sim 1.1\times 10^4$ times change in *Q* occurs with a change in *L* as small as $0.1875a$ when $L\sim -0.65a$. For $L>0$, local minima of *Q* can be seen to increase exponentially with *L*. We then compare the local minimum at $L=1.875a$ ($Q\sim 4.2\times 10^3$) with the neighboring local maximum at $L=2.125a$ ($Q\sim 6.0\times 10^6$) to investigate the cause of the remarkable oscillation. Field distributions of the two cases are shown in Fig. 11. It is clear that although *L*'s are slightly different, the intervals between the point-defect mode and the start of the line-defect mode are much different. In the high-*Q* structure, a weakly coupled state, which barely couples with the line-defect mode in a similar way to the lack of coupling in the symmetric structures studied earlier, is formed at the end of the waveguide. Strength of the point-defect mode decays exponentially with distance into the photonic crystal. Thus, *Q* increases sharply with increase of the above interval. Similar phenomena were also found in other neighboring local minima and local maxima for $L>0$. In the case of $L<0$, the light in the point defect can flow into the waveguide in *y*-axis and $-y$-axis directions. The light that flows in the *y*-axis direction is reflected at the waveguide end. The lights therefore interfere either constructively (small *Q*) or destructively (large *Q*). This interference is thought to be the cause of the oscillation in the case of $L<0$.

Two other coupling structures having a different number of rods separating the point and line defects, as shown in Figs. 12(a) and 12(b), were also investigated. Figure 13 shows *Q* plotted as a function of *L* for structures in which the defects are on neighboring rods (a) and on rods separated by two intervening rods (b). In the case of Fig. 13(a), the in-plane size of the photonic crystal is $19a\times 53a$ for $L\geqslant -1.5a$ and $23a\times 43a$ for $L<-1.5a$, respectively. The center of the point defect is located at $(9.5a,-9.5a)$ and $(11.5a,-12.5a)$, respectively, where the coordinate origin is the upper left corner of the photonic crystal. In the case of

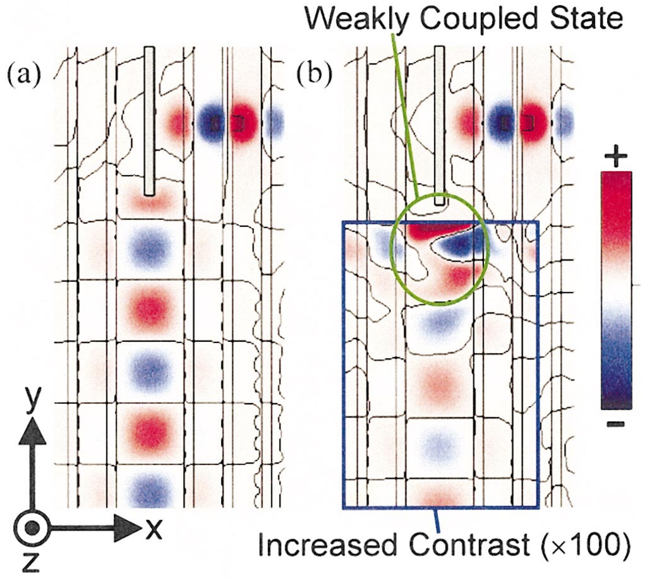

FIG. 11. (Color) Distribution of the electric field E_z across the middle of the defect layer in the structure shown in Fig. 10(a), (a) in the case of $L=1.875a$ ($Q\sim4.2\times10^3$) and (b) in the case of $L=2.125a$ ($Q\sim6.0\times10^3$). Contour lines indicate $E_z=0$. The color bar shows the field strength ranging from $-M$ to $+M$, where $M=\max(|E_z|)$. In the region framed by the blue line, the contrast of the color plot has been increased, and the color bar corresponds to the field strength ranging from $-M/100$ to $+M/100$.

Fig. 13(b), the in-plane size and the position of the point defect are $23a\times43a$ and $(12.5a,-12.5a)$. In Fig. 13(a), data for the cases $L=-2.5a$, $-1.0a$, and $-0.25a$ are omitted. For $L=-2.5a$, the point-defect mode behaves in a multimode rather than single-mode fashion. In the other cases ($L=-1.0a,-0.25a$), values of Q are so small that reliable data could not be obtained.

Results of the three asymmetric structures are compared. Oscillations in Q are common to all of the structures; however, the periodicity of L for Q oscillations is different among the structures. We then attempt to find the origin of this periodicity. We suppose that the oscillations are related to the field distribution of the point-defect mode for $L>0$. Positions of the waveguide end that produce local maxima in Q are plotted against the spatial distribution of the point-defect mode in Fig. 14. It can be seen that the intervals correspond to almost half a cycle of the point-defect mode. The local field pattern appears to be quite similar every half cycle. We consider that the cause of the periodicity of L is due to the repetitive structure of the point-defect mode when $L>0$. Moreover, we describe the case of $L<0$, illustrated by the field patterns shown in Fig. 15. It can be seen that the resonant mode is not only distributed throughout the point defect but also along the line defect from the end of the waveguide to approximately $L=0$. As L changes, the localized field around the end of the waveguide changes, while the localized field in the point defect remains similar. We suppose that the periodicity is related to localization around the end of the waveguide. In Figs. 15(a)–15(d), field patterns at local maxima of Q are shown for the structure in which the

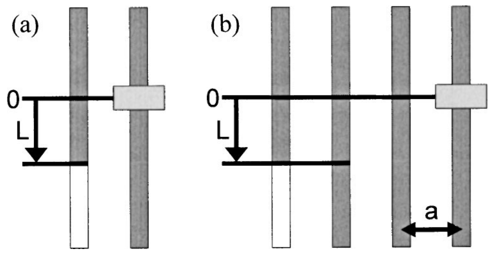

FIG. 12. Schematic of structures with a point-defect cavity and a line-defect waveguide (a) on the neighboring rod and (b) on the third neighboring rod. L is a measure of the waveguide position.

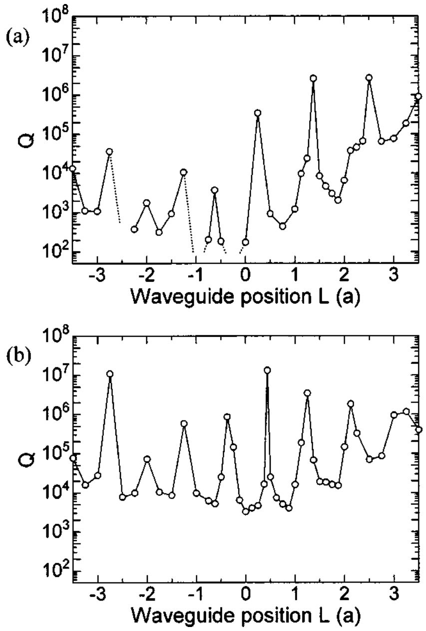

FIG. 13. Quality factor as a function of the waveguide position L for (a) the structure shown in Fig. 12(a) and (b) the structure shown in Fig. 12(b).

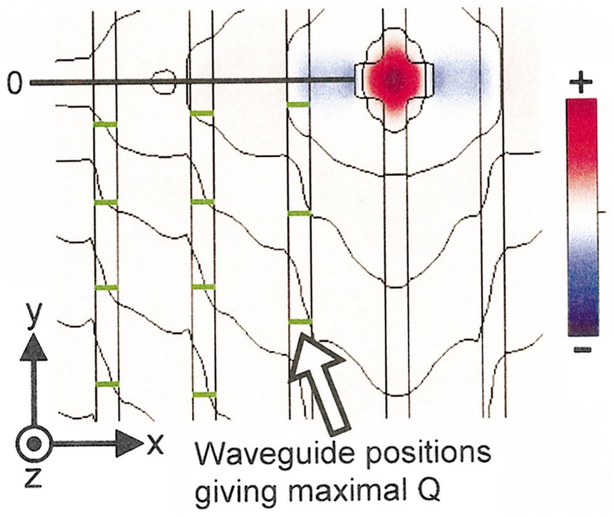

FIG. 14. (Color) Waveguide locations (green lines) that produced local maxima in Q are plotted on a map of the magnetic field H_z of the point-defect mode. Contour lines indicate $H_z=0$.

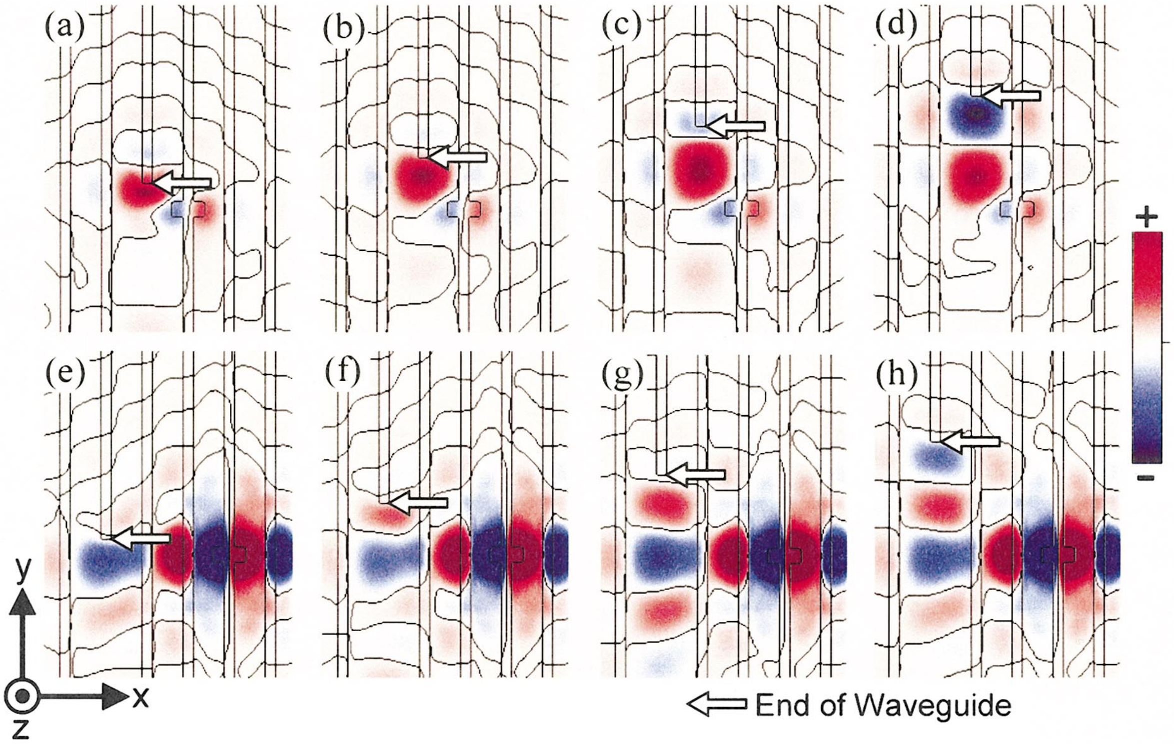

FIG. 15. (Color) Distribution of the electric field E_z across the middle of the defect layer in cases where Q is locally maximal and $L<0$. (a)–(d) are for the structure shown in Fig. 12(a), and (e)–(h) are for the structure shown in Fig. 12(b). Contour lines indicate $E_z=0$. In (e)–(h), the contrast of the color plot has been increased. The color bar corresponds to field strengths from $-M/5$ to $M/5$, where $M=\max(|E_z|)$.

waveguide is introduced into the rod neighboring the point defect. As the absolute value of L becomes larger, field E_z at the end of the waveguide (strictly speaking, at the position slightly above from the end of the waveguide) alternates between the antinode and node. This result indicates that the periodicity of L corresponds to a quarter cycle of the localized field around the end of the waveguide when $L<0$. Spacings between local maxima of Q in this structure were $0.625a$, $0.75a$, and $0.75a$, in good agreement with the quarter period of the line-defect mode of $\sim 0.8a$. Localized states around the end of the waveguide appear to be based on the line-defect mode. Similar results are obtained for structures with the waveguide located on the second neighboring rod from the point defect. However, when the waveguide is located on the third neighboring rod, slightly different results are produced, as shown in Figs. 15(e)–15(h). The field E_z at the end of the waveguide changes into node, node, antinode, and node as the absolute value of L increases. Node states persist because localization around the end of the waveguide is weak, as shown in Figs. 15(e) and 15(f). In this case periodicity of L does not correspond to a quarter period of the localized state around the end of the waveguide.

D. Asymmetric structure for light extraction in the extra direction

Next, extraction of light from the crystal in a different direction from the one previously described is explored for allowing more flexible application to optical circuits. We assume that a light emitter is introduced into only a single layer. Under this assumption, the point defect needs to be placed in the light-emitter layer, while the line-defect waveguide can be located arbitrarily. The structure shown in Fig. 16(a), in which the line-defect waveguide has been moved to the neighboring layer, is therefore considered. Light is then extracted in the normal direction to the previous one.

Q as a function of the location of the waveguide, L, is shown in Fig. 16(b) for values of L from $0.5a$ to $4.5a$. The in-plane size of the photonic crystal is $43a\times 23a$. The center of the point defect is sited at $(12.5a,-11.25a)$, when the coordinate origin is the upper left corner of the photonic crystal. For $L<0.75a$, values of Q are too small for reliable data to be acquired. Results are similar to those found in the original structures.

E. Structures with a finite size of the photonic crystal

In the preceding sections, the size of the photonic crystal was large enough to render radiation losses negligible. In this section, the effect of the size (radiation losses) on the quality factor and light extraction efficiency is considered in order to develop guiding principles that should be applied to experimental work. The total quality factor Q_{T} and light extraction efficiency η can be expressed as

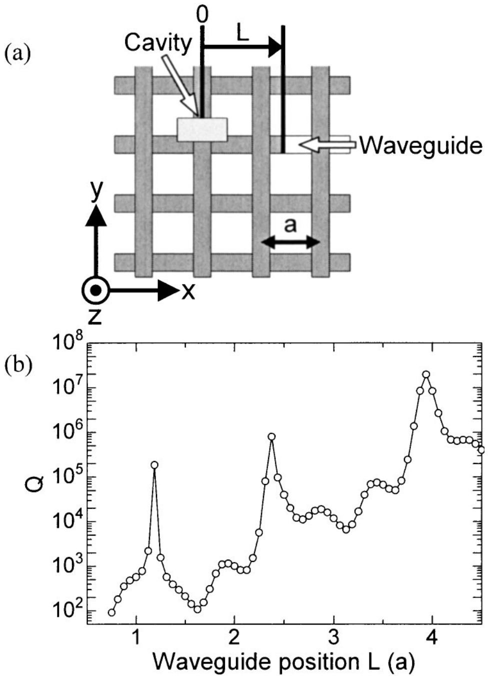

FIG. 16. (a) Schematic of structure where the waveguide is in the neighboring layer to the point defect. *L* is defined as the location of the waveguide as shown. (b) Quality factor as a function of *L* for the structure in (a).

$$\frac{1}{Q_{\mathrm{T}}}=\frac{1}{\omega_0}\frac{\text{power loss}}{\text{stored energy}}=\frac{1}{\omega_0}\frac{P(t)}{U(t)}=\frac{1}{\omega_0}\frac{P_{\mathrm{wg}}(t)+P_{\mathrm{loss}}(t)}{U(t)}$$

$$=\frac{1}{\omega_0}\frac{p_{\mathrm{wg}}(t)}{U(t)}+\frac{1}{\omega_0}\frac{P_{\mathrm{loss}}(t)}{U(t)}=\frac{1}{Q_{\mathrm{wg}}}+\frac{1}{Q_{\mathrm{loss}}}, \tag{7}$$

$$\eta=\frac{P_{\mathrm{wg}}(t)}{P_{\mathrm{wg}}(t)+P_{\mathrm{loss}}(t)}=\frac{\dfrac{1}{\omega_0}\dfrac{P_{\mathrm{wg}}(t)}{U(t)}}{\dfrac{1}{\omega_0}\dfrac{P_{\mathrm{wg}}(t)+P_{\mathrm{loss}}(t)}{U(t)}}$$

$$=\frac{Q_{\mathrm{T}}}{Q_{\mathrm{wg}}}=\frac{Q_{\mathrm{loss}}}{Q_{\mathrm{wg}}+Q_{\mathrm{loss}}}. \tag{8}$$

$U(t)$ is stored energy in the point defect, P_{wg}(t) is the amount of power transferred from the point defect to the waveguide, and P_{loss}(t) is the amount of power radiated out of the photonic crystal due to the finite size of the crystal. Q_{wg} and Q_{loss} can then be defined as

$$Q_{\mathrm{wg}}=\omega_0\frac{U(t)}{P_{\mathrm{wg}}(t)},\quad Q_{\mathrm{loss}}=\omega_0\frac{U(t)}{P_{\mathrm{loss}}(t)}. \tag{9}$$

In addition, P_{loss}(t) and Q_{loss} are expressed as

$$P_{\mathrm{loss}}(t)=P_{+x}(t)+P_{-x}(t)+P_{+y}(t)+P_{+z}(t)+P_{-z}(t), \tag{10}$$

$$\frac{1}{Q_{\mathrm{loss}}}=\frac{1}{Q_{+x}}+\frac{1}{Q_{-x}}+\frac{1}{Q_{+y}}+\frac{1}{Q_{+z}}+\frac{1}{Q_{-z}}, \tag{11}$$

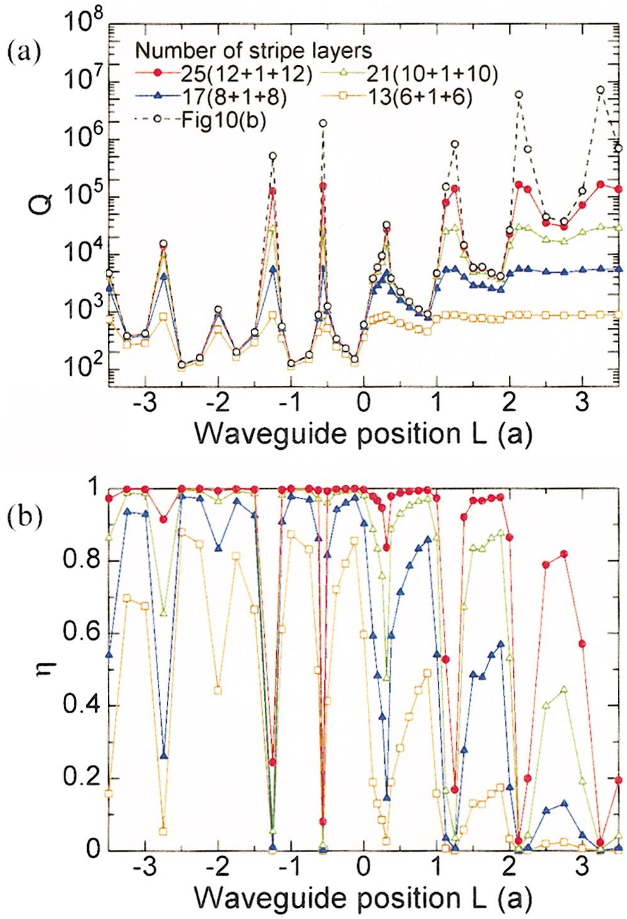

FIG. 17. (Color) (a) Dependence of quality factor of the structure shown in Fig. 10(a) on waveguide position *L* and number of stripe layers. (b) Dependence of light extraction efficiency η of the structure shown in Fig. 10(a) on waveguide position *L* and number of stripe layers.

$$Q_i=\omega_0\frac{U(t)}{P_i(t)}\quad(i=\pm x,+y,\pm z). \tag{12}$$

$P_{\pm x}(t)$, $P_{+y}(t)$, and $P_{\pm z}(t)$ are the radiation power through *yz*, *zx*, and *xy* planes that surround the photonic crystal, where the waveguide is formed in the $-y$-axis direction.

When the size of the photonic crystal is enough large, as was the case for the data presented, Q_{T} is regarded as Q_{wg} ($\eta\sim 1$). The values of *Q* shown in Figs. 10(b), 13, and 16(b) are therefore equivalent to Q_{wg}. In contrast, when no waveguide exists, Q_{T} is taken to be Q_{loss} ($\eta\sim 0$). Q_{loss} can be estimated by using the *Q*'s shown in Fig. 3, where Q_i ($i=\pm x,+y,\pm z$) corresponds to $2Q$ in the equivalent direction. Therefore Q_{T} and η in a general structure can be evaluated from values of Q_{wg} and Q_{loss}.

In many experimental cases, 3D photonic crystal called a layer-by-layer structure has a small number of stripe layers and a large in-plane size. Thus, the effect of the vertical size on Q_{T} and η is especially important. For a significant example, the dependence of Q_{T} and η on the number of stripe layers in the structure shown in Fig. 10(a) is plotted in Fig. 17. As the number of layers decreases, both Q_{T} and η de-

TABLE I. Comparison between estimated and real total quality factor Q_{T} of the structure shown in Fig. 10(a) with $L=1.75a$. The number of stripe layers varies from $13(6+1+6)$ to $25(12+1+12)$. Estimated Q_{T} is calculated from Eq. (7). Q_{wg} and Q_{loss} are shown in Figs. 10(b) and 3, respectively. Real Q_{T} is calculated in an actual structure with a finite number of stripe layers.

Number of stripe layers	Estimated Q_{T}	Real Q_{T}	Difference (%)
$13(6+1+6)$	743.1	742.4	0.094
$17(8+1+8)$	2551	2551	-
$21(10+1+10)$	4085	4086	0.024
$25(12+1+12)$	4606	4607	0.022

crease. Note that in the above discussion, it was assumed that Q_{wg} depends solely on the position of the waveguide and that Q_{loss} is dependent solely on the size of the photonic crystal [to be exact, Q_i $(i=\pm x,+y,\pm z)$ is dependent only on the corresponding size of the photonic crystal].

In reality, Q_{wg} and Q_{loss} also depend on the size of the crystal and the waveguide position, respectively, although on the whole these dependences seem insignificant. We verify the above assumptions for a typical structure with a finite number of stripe layers and a large in-plane size. Q_{T} of the structure shown in Fig. 10(a) with L equal to $1.75a$ was directly calculated as a function of the number of stripe layers. We call this Q_{T} "real Q_{T}" and the above Q_{T}, which is estimated from values of Q_{wg} and Q_{loss}, "estimated Q_{T}." The differences between the estimated Q_{T} and the real Q_{T} are shown in Table I and are extremely small ($<0.1\%$). It is confirmed that the above assumptions are acceptable.

V. CONCLUSION

Coupling properties of a point-defect cavity and a line-defect waveguide in 3D photonic crystal were analyzed theoretically. A symmetric structure in which the point and line defects were in the same rod was found to result in no coupling between the defect modes due to a mismatch in parity of the defect modes around the plane of symmetry. A coupling state can be formed by introducing asymmetry into the structure. For the four asymmetric structures considered, the coupling strengths of the point- and line-defect modes were estimated as a function of the position of the waveguide by measuring the quality factor Q of the point defect. Q was found to oscillate with small changes in the position of the waveguide, with Q changing as much as $\sim 1.1\times 10^4$ times with a change in position as small as $0.1875a$. It is a very interesting physical phenomenon. We believe that this feature will be applicable to various applications, such as Q switching, through the introduction of material with a refractive index that can be dynamically controlled into the photonic crystal. Furthermore, Q and light extraction efficiency were estimated for a photonic crystal with a finite size, to approximate experimental conditions. The findings have revealed very useful design rules for controlling the transfer of light from the point defect to the waveguide. These coupling structures are thought to have importance as components in 3D photonic crystal optical circuits.

ACKNOWLEDGMENTS

This work was supported in part by CREST, JST, 21COE of Kyoto University, Grant-in-Aid for Scientific Research, and IT Program from MEXT.

---

*Corresponding author. Email address: mokano@qoe.kuee.kyoto-u.ac.jp

[†]Corresponding author. Email address: snoda@kuee.kyoto-u.ac.jp

[1] E. Yablonovitch, Phys. Rev. Lett. **58**, 2059 (1987).

[2] S. John, Phys. Rev. Lett. **58**, 2486 (1987).

[3] S. Noda, K. Tomoda, N. Yamamoto, and A. Chutinan, Science **289**, 604 (2000).

[4] S. Noda, A. Chutinan, and M. Imada, Nature (London) **407**, 608 (2000).

[5] E. Yablonovitch, T. J. Gmitter, R. D. Meade, A. M. Rappe, K. D. Brommer, and J. D. Joannopoulos, Phys. Rev. Lett. **67**, 3380 (1991).

[6] Robert D. Meade, Karl D. Brommer, Andrew M. Rappe, and J. D. Joannopoulos, Phys. Rev. B **44**, 13 772 (1991).

[7] E. M. Purcell, Phys. Rev. **69**, 681 (1946).

[8] D. Kleppner, Phys. Rev. Lett. **47**, 233 (1981).

[9] S. Noda, N. Yamamoto, M. Imada, H. Kobayashi, and M. Okano, J. Lightwave Technol. **17**, 1948 (1999).

[10] K. M. Ho, C. T. Chan, C. M. Soukoulis, R. Biswas, and M. Sigalas, Solid State Commun. **89**, 413 (1994).

[11] E. Özbay, E. Michel, G. Tuttle, R. Biswas, M. Sigalas, and K. M. Ho, Appl. Phys. Lett. **64**, 2059 (1994).

[12] H. S. Sözüer and J. P. Dowling, J. Mod. Opt. **41**, 231 (1994).

[13] S. Noda, N. Yamamoto, and A. Sasaki, Jpn. J. Appl. Phys., Part 2 **35**, L909 (1996).

[14] S. Noda, M. Imada, M. Okano, S. Ogawa, M. Mochizuki, and A. Chutinan, IEEE J. Quantum Electron. **38**, 726 (2002).

[15] M. Okano, A. Chutinan, and S. Noda, Phys. Rev. B **66**, 165211 (2002).

[16] A. Chutinan and S. Noda, Appl. Phys. Lett. **75**, 3739 (1999).

[17] M. M. Sigalas, R. Biswas, K. M. Ho, C. M. Soukoulis, D. Turner, B. Vasiliu, S. C. Kothari, and S. Lin, Microwave Opt. Technol. Lett. **23**, 56 (1999).

[18] A. Chutinan and S. Noda, Jpn. J. Appl. Phys., Part 1 **39**, 2353 (2000).

[19] M. Bayindir, E. Ozbay, B. Temelkuran, M. M. Sigalas, C. M. Soukoulis, R. Biswas, and K. M. Ho, Phys. Rev. B **63**, 081107 (2001).

[20] M. Bayindir and E. Ozbay, Appl. Phys. Lett. **81**, 4514 (2002).

[21] K. M. Leung and Y. F. Liu, Phys. Rev. Lett. **65**, 2646 (1990).

[22] Z. Zhang and S. Satpathy, Phys. Rev. Lett. **65**, 2650 (1990).

[23] K. S. Yee, IEEE Trans. Antennas Propag. **AP-14**, 302 (1966).

[24] *Photonic Band Gaps and Localization*, edited by C. M. Soukoulis, in *Proceedings of the NATO Advanced Science Institutes Series* (Plenum, New York, 1993), p. 235.

[25] J.-P. Berenger, J. Comput. Phys. **114**, 185 (1994).

[26] D. S. Katz, E. T. Thiele, and A. Taflove, IEEE Microwave Guid. Wave Lett. **4**, 268 (1994).

[27] M. Koshiba, Y. Tsuji, and M. Hikari, J. Lightwave Technol. **18**, 102 (2000).

[28] M. Koshiba, Y. Tsuji, and S. Sasaki, IEEE Microw. Wirel. Compon. Lett. **4**, 152 (2001).

[29] J. B. Verdu, R. Gillard, K. Moustadir, and J. Citerne, Microwave Opt. Technol. Lett. **10**, 323 (1995).

[30] M. Okano and S. Noda (unpublished).

[31] P. R. Villeneuve, S. Fan, and J. D. Joannopoulos, Phys. Rev. B **54**, 7837 (1996).

[32] J. D. Jackson, *Classical Electrodynamics*, 3rd ed. (Wiley, New York, 1999).